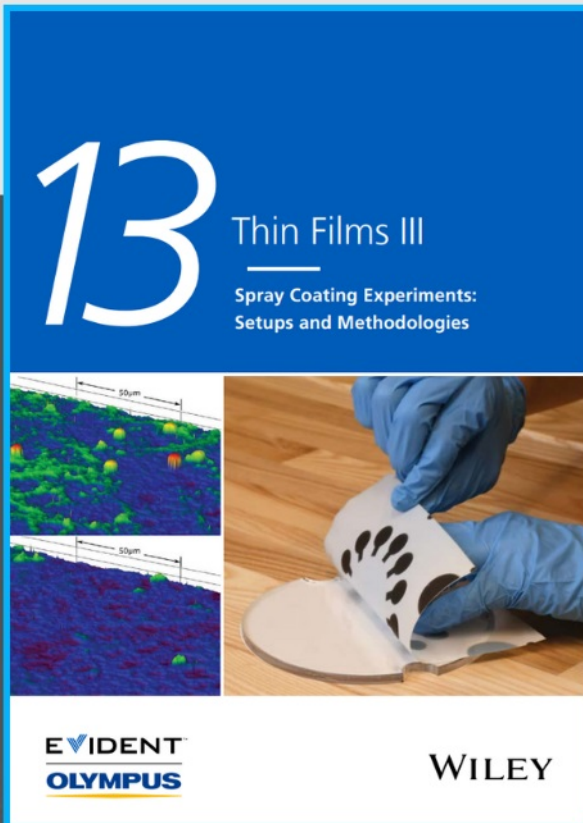# Spray Coating Experiments: Setups and Methodologies

The latest eBook from Advanced Optical Metrology. Download for free.

Spray Coating Experiments: Setups and Methodologies, is the third in our Thin Films eBook series. This publication provides an introduction to spray coating, three article digests from Wiley Online Library and the latest news about Evident's Image of the Year Award 2022.

Wiley in collaboration with Evident, are committed to bridging the gap between fundamental research and industrial applications in the field of optical metrology. We strive to do this by collecting and organizing existing information, making it more accessible and useful for researchers and practitioners alike.

13 Thin Films III

Spray Coating Experiments: Setups and Methodologies

EVIDENT OLYMPUS   WILEY

EVIDENT OLYMPUS

WILEY

Influences of Partial Destruction of Ti-MOFs on Photo(electro)catalytic H$_2$ Evolution by Dominating Role of Charge Carrier Trapping over Surface Area

Aslam Hossain, M. S. Meera, E. A. Mukhanova, A. V. Soldatov, A. M. A. Henaish, Jahangeer Ahmed, Yuanbing Mao, and S. M. A. Shibli*

The design of water-stable photo and electrocatalysts of metal–organic frameworks (MOFs) for its promising catalytic applications at long-term irradiations or persisted current loads is extremely necessary but still remains as challenging. A limited number of reports on Ti-MOF-based catalysts for water splitting are only available to explain and understand the correlation between the nature of materials and MOFs array. Herein, spherical Ti-MOFs and corresponding partially annealed hollow core–shell Ti-MOFs (Ti-MOF/D) are designed and the correlation with their photo(electro)catalytic water splitting performance is evaluated. The switchable valence state of Ti for the Ti-MOF as a function of molecular bonding is the possible reason behind the observed photocatalytic hydrogen generation and light-harvesting ability of the system. Besides, the defect state, solid core–shell mesoporous structure, and active sites of Ti-MOF help to trap the charge carriers and the reduction of the recombination process. This phenomenon is absent for hollow core–shells Ti-MOF/D spheres due to the rigid TiO$_2$ outer surface although there is a contradiction in surface area with Ti-MOF. Considering the diversity of Ti-MOF and Ti-MOF/D, further novel research can be designed using this way to manipulate their properties as per the requirements.

1. Introduction

The skeleton of metal and organic ligands appears as versatile porous materials used in an extensive range of applications.[1] Typically, metal–organic frameworks (MOFs) are considered poor catalysts for hydrogen evolution reaction (HER) by water spitting where several factors can be used to optimize this property such as metal active sites, electrical conductivity, and specific morphology.[2] The optimization of these parameters is crucial to enhance the efficiency of MOF catalysts but it is a difficult task without compromising one or the other. Taking into account that MOFs are plentiful for intrinsic molecular metallic sites but few are used as catalytic sites due to their small pore size and high electrical resistance.[1b,3]

The morphology and specific shape and size of the particles of materials can greatly affect their properties.[4] The mesoporous hollow core–shell structure has attracted significant attention due to the superior advantages when compared with the solid structure. The advantages of hollow structures include:[5] i) the catalytic reactions can be selectively enhanced by molecular sieving if pore size is properly optimized, ii) eligible to mass transfer throughout the shell wall, and iii) reaction rates of reagents can be increased in the voids to. Recently, intricate hollow structures have attracted attention not only from fundamental aspects but also to create materials with higher degree of complexity and appealing

A. Hossain, E. A. Mukhanova, A. V. Soldatov
Smart Materials Research Institute
Southern Federal University
Sladkova 178/24, Rostov-on-Don 344090, Russia

M. S. Meera, S. M. A. Shibli
Department of Chemistry
University of Kerala
Kariavattom Campus, Thiruvananthapuram, Kerala 695 581, India
E-mail: smashibli@yahoo.com

A. M. A. Henaish
Physics Department
Faculty of Science
Tanta University
Tanta 31527, Egypt

A. M. A. Henaish
NANOTECH Center
Ural Federal University
Ekaterinburg 620002, Russia

J. Ahmed
Department of Chemistry
College of Science
King Saud University
P.O. Box 2455, Riyadh 11451, Saudi Arabia

Y. Mao
Department of Chemistry
Illinois Institute of Technology
Chicago, IL 60616, USA

S. M. A. Shibli
Centre for Renewable Energy and Materials
University of Kerala
Kariavattom Campus, Thiruvananthapuram, Kerala 695 581, India

**ADVANCED
SCIENCE NEWS**
www.advancedsciencenews.com

**NANO · MICRO
small**
www.small-journal.com

beauty to meet application demands.[6] Intricate hollow structures having noticeable properties such as low density, large specific surface area, reduced mass/charge diffusion lengths leading to interesting modern applications.[6] This specific morphology offers more opportunities to tune their properties by manipulating the structure at micro/nanoscale compared with others. However, the construction of similar intricate structures is still remain as challenging.

Concerning photo(electro)catalytic properties, hollow structures have exceptional advantages over their solid counterparts due to their aesthetic shell layer. The boosted specific surface area and promoted surface redox reactions on both sides of hollow structured shell walls promote charge migration and separation.[7] The described merits make these materials an ideal candidate to design an elaborate catalytic system for HER.

Among various possible strategies for hollow structures, annealing MOFs at high temperatures may lead to reducing their intrinsic metal active sites and block their intrinsic micropores whereas bulk material has limited to meso/macroporosity for effective mass transport during electrocatalysis.[8] The aim of our current study is to tune the catalytic properties Ti-MOF by partial decomposition of its organic counterpart by forming hollow structures of TiO$_2$. Many efforts have been made to enhance the catalytic properties of TiO$_2$ using ion doping, coexistence of anatase-rutile phase, morphology tuning, etc.[9] Interestingly, our designed hollow structure by partial decomposition of an organic moiety of preformed Ti-MOFs by low-temperature annealing for few a minutes shows unusual catalytic activity compared with those reported in the literature. We have analyzed and verified the formation mechanism and have explained in detail the reason behind the unusual activities.

Specifically, we developed spherical Ti-MOFs via the interaction between salicylate ligand and the corresponding Ti ions in the absence of polymeric reagents and then designed hollow core–shell Ti-MOF/D using low-temperature annealing of the as-synthesized MOFs (**Figure 1**a). We have proposed the formation mechanism of core–shell hollow structure of Ti-MOF/D based on the combined data of X-ray photoelectron spectroscopy (XPS) and UV–vis spectra. The obtained Ti-MOF photocatalyst solid sphere shows HER two times higher than that of Ti-MOF/D though the surface area is seven times higher for Ti-MOF/D. Similarly, electrocatalytic HER activity was also reduced for Ti-MOF/D which is explained on the basis of experimental evolution. Based on XPS and optical data, we have proposed the formation mechanism and light absorption mechanism of Ti-MOF and Ti-MOF/D. Further, we have proposed the photocatalytic mechanism of Ti-MOF by switching between Ti^{3+}/Ti^{4+} evaluated by XPS and photophysical properties.

2. Results and Discussions

2.1. Design and Formulation

The Ti-based MOF and its partial annealed materials were investigated utilizing a photo(electro)catalytic HER and the effect of the destruction of the MOF structure was evaluated.
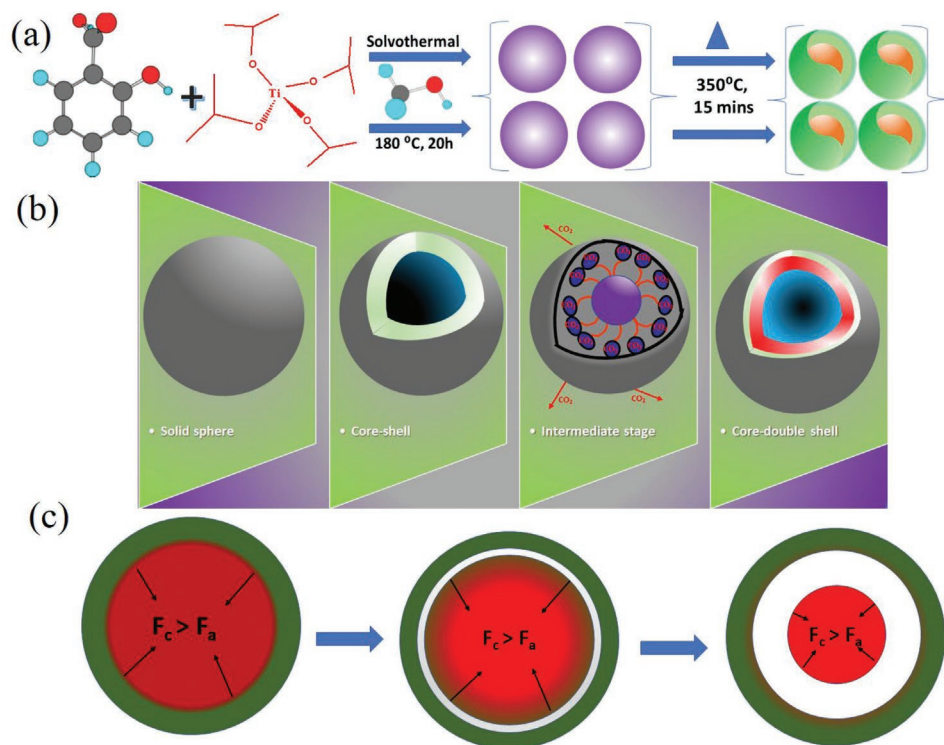

Figure 1. Schematic illustration of the Ti-MOF and Ti-MOF/D formation process. a) Preparation of perfect spherical Ti-MOF using the solvothermal method of titanium isopropoxide with salicylic acid and then Ti-MOF/D by annealing. b) Step-by-step conversion of spherical Ti-MOF into hollow Ti-MOF/D sphere when calcined at 350 °C for 15 min. c) The primary driving force for the formation of such hollow structures of Ti-MOF/D.

The perfect spherical Ti-MOF was grown using a solvothermal method and Ti-MOF/D was prepared in a controlled air-annealing atmosphere as shown in Figure 1. Initially, the Ti-precursor was combined through the coordination interaction with salicylate ligands (Figure 1a) through strong bind of –COOH functional groups and thus created nuclei sites for the growth of Ti-MOF. This is a universal method for transition metals due to the nonselectivity nature of salicylic acid.[8,10] Subsequently, in the second step, Ti-MOF was controlled annealing at 350 °C for 15 min to partially decompose the organic ligand by forming a hybrid core–shell nanostructure. The second step is crucial to modify TiO_2 surface to promote the photo(electro) catalytic activity of the Ti-MOF/D hollow structure.

2.2. Physicochemical Characterizations

2.2.1. Evaluation of Crystallinity of Ti-MOFs and Ti-MOF/D

The study of X-ray diffraction (XRD) confirms well crystallinity nature of Ti-MOF/D compared with pure Ti-MOF shown in Figure S1 in the Supporting Information. The comparative study of Fourier transform infrared spectroscopy (FTIR) spectra of salicylic acid and Ti-MOF is evidence of the interaction among the deprotonated carboxylate groups in salicylate ligands and Ti ions (Figure S1b, Supporting Information). This interaction can be confirmed by the comparison of C=O peak at 1653 cm^{-1} for salicylic acid which had a redshift at 1600 cm^{-1} for Ti-MOF.[11] Sayed et al. claimed that acetate anions (conjugate base) can deprotonate the carboxylate groups in salicylic acid while the replacement of metal acetate by metal sulfide, nitrates, or chlorides failed to fabricate such spherical architecture.[8] Unlike their claim, we have used Ti-isopropoxide as a precursor in the absence of polyvinylpyrrolidone for the fabrication of perfect spherical particles confirming the ability of the isopropoxide anion to deprotonate carboxylate groups of salicylic acid.

In the second step, the partial decomposition of the organic ligand can generate hollow structures by heterogeneous contraction (Figure 1b,c).[8] In the beginning, both the core and the newly developed shell experienced two opposite forces, responsible for the formation of varieties of architecture at different stages. These are the inward cohesion force (F_c) and outward adhesion force (F_a) originating from the shrinkage of the interior core by continuous decomposition of the carbon content organic moiety and emanating from the cling of adjacent crystallites respectively. Primarily, at a smaller temperature gradient, F_c greater than F_a leads to the separation of the entire core from the outer shell forming the unique hollow sphere (Figure 1c). It is important to note that the present organic moiety in both the inner layer and the outer layer decomposes during annealing, leading to the formation of pores that allow the mass transfer of the reactants/products.[12] The elemental analysis supports the partial decomposition of the organic ligand while the carbon content of T-MOF and Ti-MOF/D is 29.64% and 10.37%, respectively (Table S1, Supporting Information). This unique nature of the hollow sphere can trap the incident light and decrease the recombination rate of photogenerated charge carriers.[8]

All the Ti-MOF particles have a smooth surface texture and highly uniform solid spheres with varieties of diameters from 5 to 8 μm, evaluated from transmittance electron microscopy (TEM) images (**Figure 2**a,b). The Ti-MOF/D remains spherical (Figure 2g) but the diameter is dramatically expanded which could be due to the release of CO_2 by the partially decomposed organic ligand (Table S1, Supporting Information). A hollow region can be noticed between the edges of the shell and the centered sphere (Figure 2h) from a broken shell of the annealed Ti-MOFs. Figure 2d–f,j–l shows the TEM elemental mapping of Ti-MOF and Ti-MOF/D, respectively. It is clear from both images that the spherical architecture consists of Ti, C, and O atoms. The high-resolution transmission electron microscopy (HRTEM) image of the annealed sample confirmed the lattice fringe at 0.351 and 0.322 nm corresponding to the (101) plane of anatase and rutile structure of TiO_2, respectively (Figure 2i).[13]

Field emission scanning electron microscopy (FESEM) has also been carried out to clarify the evolution mechanism of the spherical architecture morphology of the Ti-MOF and Ti-MOF/D shown in **Figure 3**. Initially, the surface of the Ti-MOF sphere particle was comparatively smoother than the annealed one. The broken outer shell of the Ti-MOF/D confirms and agrees the TEM image that the presence of the hollow shell of the inner layer (Figure 3f). The annealing at 350 °C for 15 min highly influences the outermost surface of the Ti-MOF by abrupt heating is shown in Figure 3g–i. FESEM images also demonstrate the possibility of the outermost surface originating from the rigid higher concentration of TiO_2 while the inner shell might be associated with the higher organic moiety. The porosity of the inner core and outer layer can clearly distinguish the rigidity and support the claimed statement (Figure 3g–i). The annealing of Ti-MOF leads to decomposing inner organic moiety resulting in the shrinkage of the inner layer and slight expansion of the rigid outer layer by the pushing of produced CO_2. The continuous shrinkage of the entire core by annealing due to the decomposition of organic moieties is called heterogeneous contraction.[14]

Additionally, we have carried out dynamic light scattering (DLS) measurements for Ti-MOF and Ti-MOF/D to evaluate the size distribution of the synthesized particles is shown in **Figure 4**a,c, respectively. The hydrodynamic averaged particle sizes obtained from DLS measurements for Ti-MOF and Ti-MOF/D are 6.2 and 7.2 μm, respectively, which agrees with the electron microscopic data. The dispersibility nature and stability feature of the prepared samples were evaluated with Zeta potential measurements (Figure 4b,d). Those particles having higher charges and smaller sizes are less favorable to combine. The obtained zeta potentials at pH 7 for the Ti-MOF and Ti-MOF/D are −22.2 and −27.9 mV, respectively. Ti-MOF has a comparatively smaller negative charge, indicating a lower stability and affinity to agglomerate with time into clusters. This result again confirms that Ti-MOF contains the carboxylic acid group. Furthermore, the Ti-MOF/D has a higher negative zeta potential that demonstrates higher stability and homogeneity due to the repulsive force among particles associated with the partially disintegrated organic group.[15]

The FESEM images show that the surface of Ti-MOF is smooth while it becomes rough with invasive pores for Ti-MOF/D (Figure 3). Again, the porous structure of the
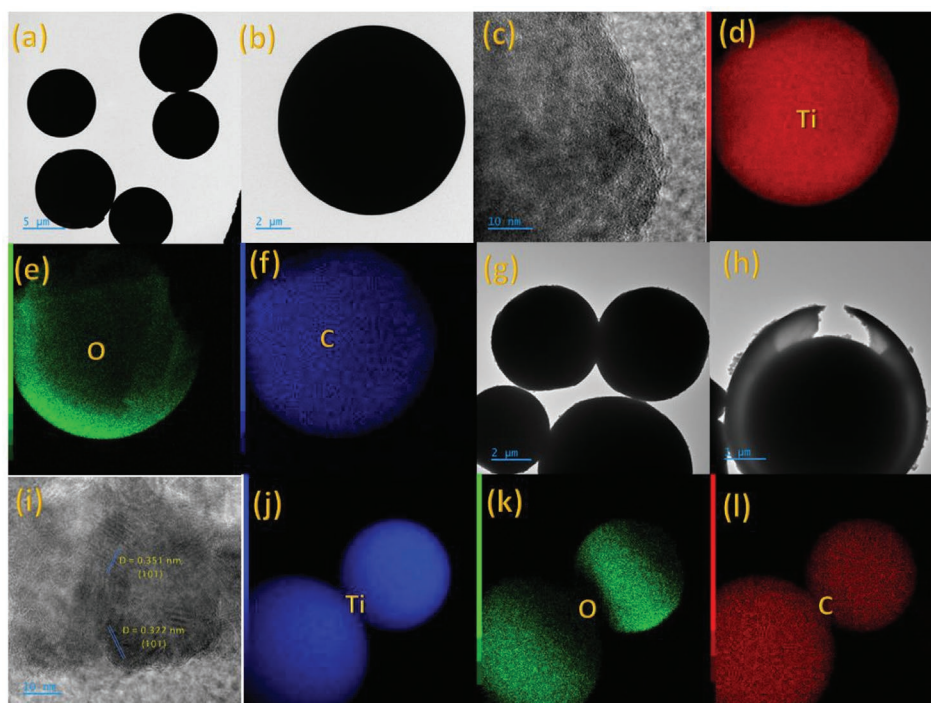
ADVANCED
SCIENCE NEWS
www.advancedsciencenews.com

NANO · MICRO
small
www.small-journal.com

Figure 2. Microstructure and elemental distribution. a–c) TEM images of Ti-MOF and g,h) Ti-MOF/D at different magnification. i) HRTEM of Ti-MOF/D with lattice fringes of 0.351 and 0.322 nm corresponds to the (101) plane of the anatase and rutile phases, respectively. (d-f) and (j–l) are the TEM elemental mapping of the Ti-MOF and Ti-MOF/D, respectively, showing the constituent elements Ti, C, and O.

samples are confirmed with nitrogen adsorption–desorption isotherm measurements and the corresponding pore size distribution curve was constructed with the Barrett–Joyner–Halenda

method (Figure 4e,f). The graph indicates a type IV isotherms with a typical mesoporous structure.[16] The diameter of the mesopores are 2.1 and 2.3 nm for Ti-MOF and the annealed
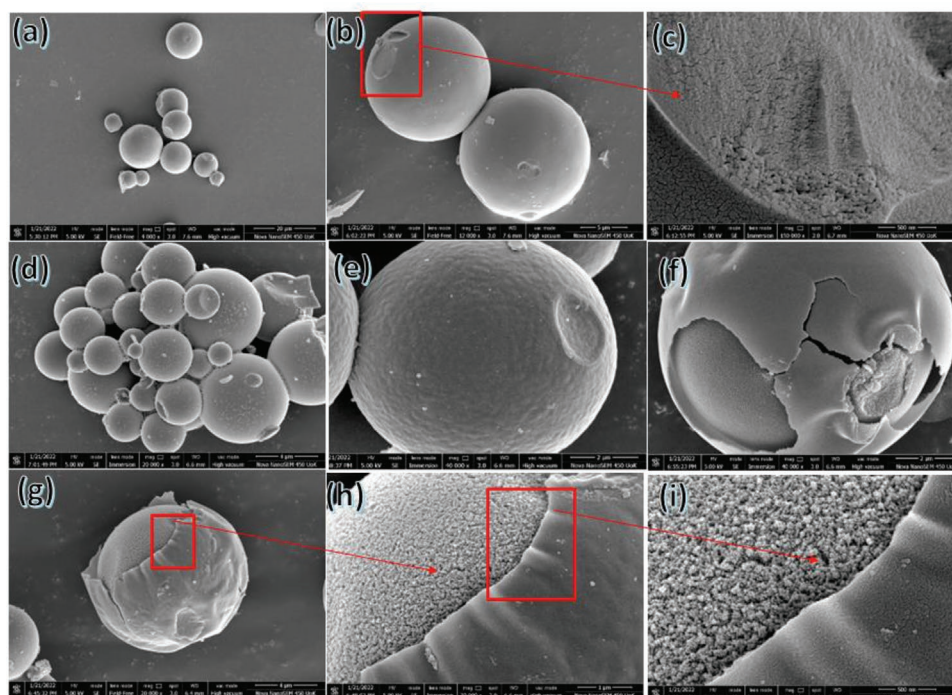

Figure 3. Morphology, inner and outer layer porosity. a–c) FESEM images of Ti-MOF and d,e) Ti-MOF/D at different magnifications. f) Broken outer shell and inner shell after annealing. g–i) Difference between the outer layer and inner shell by means of their porosity and rigidity for Ti-MOF/D at different magnifications.
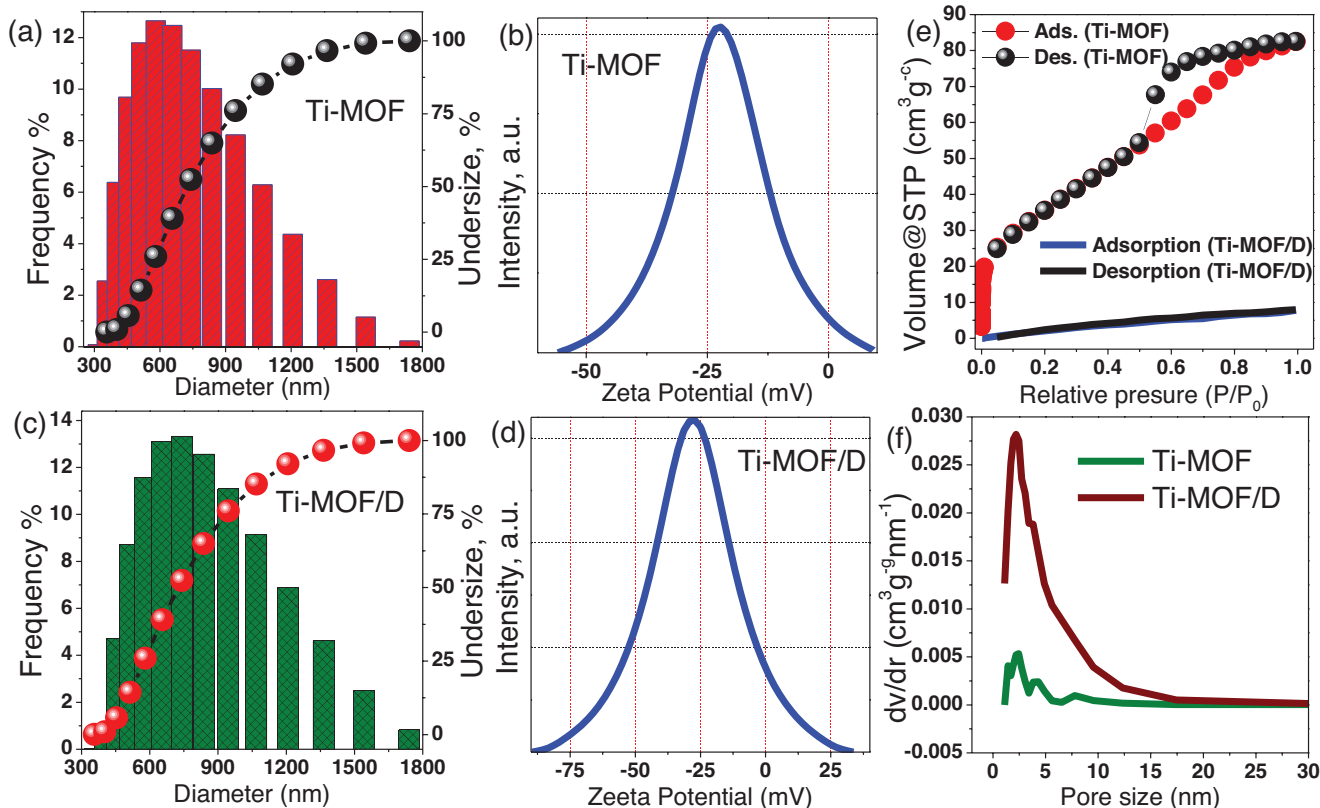
**ADVANCED
SCIENCE NEWS**

www.advancedsciencenews.com

NANO · MICRO

small

www.small-journal.com

Figure 4. Average particle size and N_2 adsorption/desorption properties: a) DLS of the Ti-MOF, b) DLS of the Ti-MOF/D, c) zeta potential of the Ti-MOF, d) zeta potential of the Ti-MOF/D, e,f) Nitrogen adsorption/desorption isotherms and the corresponding pore size distributions of Ti-MOF and Ti-MOF/D, respectively.

Ti-MOF/D sample, respectively, confirming the uniform pore size distribution (Figure 4f). The calculated Brunner–Emmet–Teller (BET) surface area of Ti-MOF/D (127.35 m^2 g^{-1}) is about seven times larger than Ti-MOF (17.72 m^2 g^{-1}). It is important to note that there is a linear relationship between the photocatalytic activity and the surface area of photocatalysts under specific conditions.[17] Besides, there is an influence of surface areas of electrodes on electrocatalytic activity as we demonstrated below.[18]

2.3. Optical Characterizations

Salicylic acid has a free phenyl group which allows a strong π–π^* transition in the UV-visible region with a high extinction coefficient. It shows bathochromic a shift of the benzenoid band at wavelength of 297 and 232 nm, respectively.[19] **Figure 5**a shows the optical absorption of Ti-MOF and the corresponding annealed Ti-MOF/D sample. One can see, the appearance of absorption peaks for Ti-MOF at 301 and 234 nm, respectively. This slight red shift might be due to the influence of Ti^{3+} ions in the MOF. In addition, the Ti-MOF could initiate other electronic transitions such as (L-M , M-L) charge transfer and d–d transition.[20] The combined effect of these transitions influences the whole system of light harvesting which leads to an enlarged absorption response.[21] In the case of the Ti-MOF, there is no typical absorption peaks appeared corresponding

to TiO_2. An ambiguous absorption band can be considered for Ti-MOF/D in the UV region of the spectrum at about 400 nm as shown in Figure 5a. This bandgap absorption is due to the electronic transitions of TiO_2 from its valence band to the conduction band ($O_{2p} \rightarrow Ti_{3d}$). There is no other optical absorption appears for the Ti-MOF/D.

The chemical state and the electronic structure of the Ti-MOF and Ti-MOF/D have been studied using XPS as shown in Figure S3 in the Supporting Information. This study confirms the presence of Ti^{3+} in the Ti-MOF along with a weak Ti—C bond whereas only Ti^{4+} is presents in the Ti-MOF/D. A detailed explanation has been provided in the Supporting Information. As per the combined data of XPS and UV–vis spectra, we have proposed the formation mechanism of the Ti-MOF/D core–shell hollow sphere as shown in Figure 5c. Initially, a unique metal–organic orientation forms in which the hydrophobic tails are in the interior of the framework while ionic Ti^{3+} ends on the surface of the framework. In the second step, the weak Ti—C and Ti—O organic bond breaks and forms a TiO_2 layer of the outer hollow sphere of the carbon content core after annealing.

Photoluminescence (PL) spectral measurements provide information such as the nature of charge carriers, its migration, conversion, and separation.[22] PL spectra revealed that suppressed charge recombination is achieved from the Ti-MOF compared with annealed Ti-MOF/D as shown in Figure 5d. The obtained lower PL intensity from the Ti-MOF is associated with
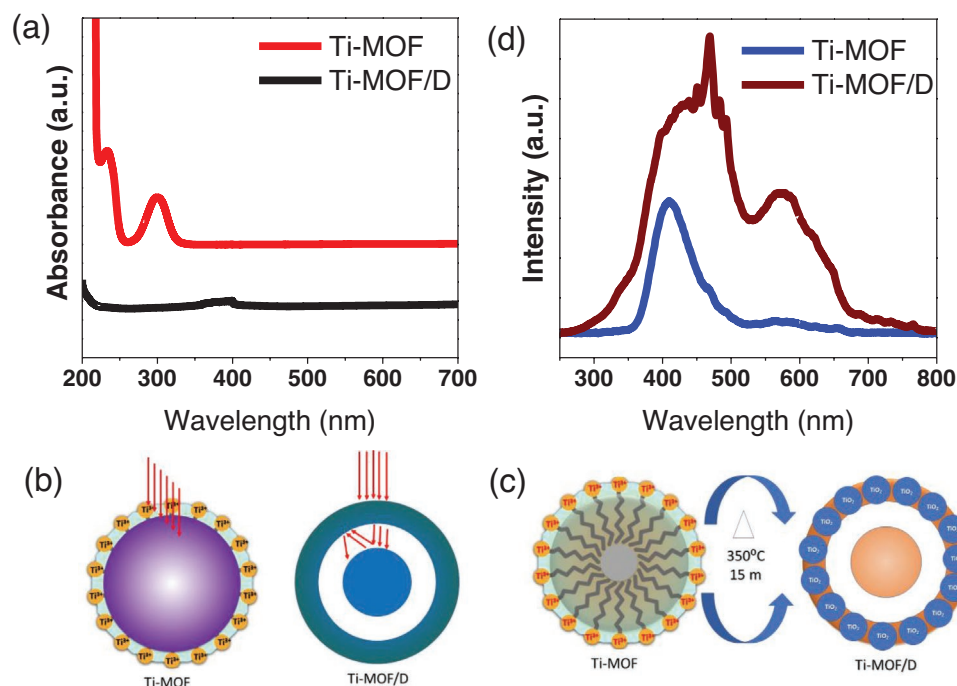
**ADVANCED
SCIENCE NEWS**

www.advancedsciencenews.com

NANO · MICRO

small

www.small-journal.com

Figure 5. Optical properties of the studied materials. a) UV–vis light absorption of the prepared MOFs. b) Multiple reflection effects of the incident light inside the Ti-MOF initiate other electronic transitions such as metal to ligand (M-L) charge transfer, ligand to metal (L-M) charge transfer and d–d transition while the reflection of the light initiated from the rigid TiO_2 layer for Ti-MOF/D. c) The proposed formation mechanism of the studied MOFs using combined data of XPS and UV–vis spectra. d) PL spectra of the Ti-MOF and Ti-MOF/D.

the defect state and solid spherical morphology along with the mesoporous structure. These help to trap the charge carriers that reduce the charge recombination process by improving the mean free path of these charge carriers.[23] The Ti-MOF/D cannot be promoted by these factors due to the rigid outer surface of TiO_2 and the hollow sphere between the outer surface and the inner core.

3. Photo(electro)catalytic HER

To authenticate the hypothesis of photocatalytic HER, the hydrogen evolution was measured over 1 h for the Ti-MOF and corresponding annealed Ti/MOF/D sample, as shown in **Figure 6**a. There was no evolution of gases at an initial 10 and 15 min for the Ti-MOF and Ti-MOF/D, respectively. Then the rate of hydrogen evolution gradually increased for both samples within the experimental time. The highest rate of hydrogen generation found as per this study was about 1616 and 713 $\mu mol\ g^{-1}\ h^{-1}$ corresponding to Ti-MOF and Ti-MOF/D, respectively (inset of Figure 6a) which is compared with literature in Table S2 in the Supporting Information. Generally, annealing of MOF at high temperatures leads to complete decomposition of the organic moieties present in both the inner and the outer layers. These decomposed organic moieties can transform into CO_2 gas and get released through the surface of the sphere resulting in creation of pores. These pores allow the mass transfer of the reactants/products. These phenomena cause enhancement of photocatalytic efficiency of the porous hollow core shell materials. In the present case, such phenomena were not adequate

to create substantial pores due to slow release of CO_2 gas. Here, the hollow core shell was generated due to the partial decomposition of the organic moieties with slow rate and the generated CO_2 gas was unable to create significant amount of pores. Thus, the created rigid outer shell of Ti-MOF/D had deficiency to utilize the solar energy appropriately to promote charge migration and separation, as evidenced by photoluminescence tests. Therefore, even though it has higher surface area, the Ti-MOF/D hollow structure showed lower photocatalytic hydrogen evolution efficiency than Ti-MOF. The apparent quantum efficiency (AQE) and hydrogen gas chromatographic results of photocatalytic hydrogen evolution for the Ti-MOF and Ti-MOF/D are shown in Figure 6b. The highest AQE obtained at 400 nm for the Ti-MOF was nearly 24.87% while that of the Ti-MOF/D showed about 10.98%.

As per the photophysical results and obtained hydrogen evolution data, we propose a catalytic cycle for the Ti-MOF photocatalytic water splitting in Figure 6c. Upon irradiation, the Ti (III)-MOF oxidized by transferring an electron. The photogenerated electron initiates the redox reaction and generated hydrogen. The zero evolution of gases at an initial 10 min indicates that strong light irradiation is required primarily to activate and generate a photoelectron. Similar observations were seen up to four photocatalytic HER runs for Ti-MOF is shown in Figure S4 in the Supporting Information. Finally, Ti(IV)-MOF is reduced by the production of O_2 and regenerates the Ti(III)-MOF. Interestingly, Ti-MOF/D required more time to activate and evaluate H_2 compared to the Ti-MOF, which could be due to the rigid outer layer of TiO_2. In this case, the present TiO_2 on the

ADVANCED
SCIENCE NEWS
www.advancedsciencenews.com
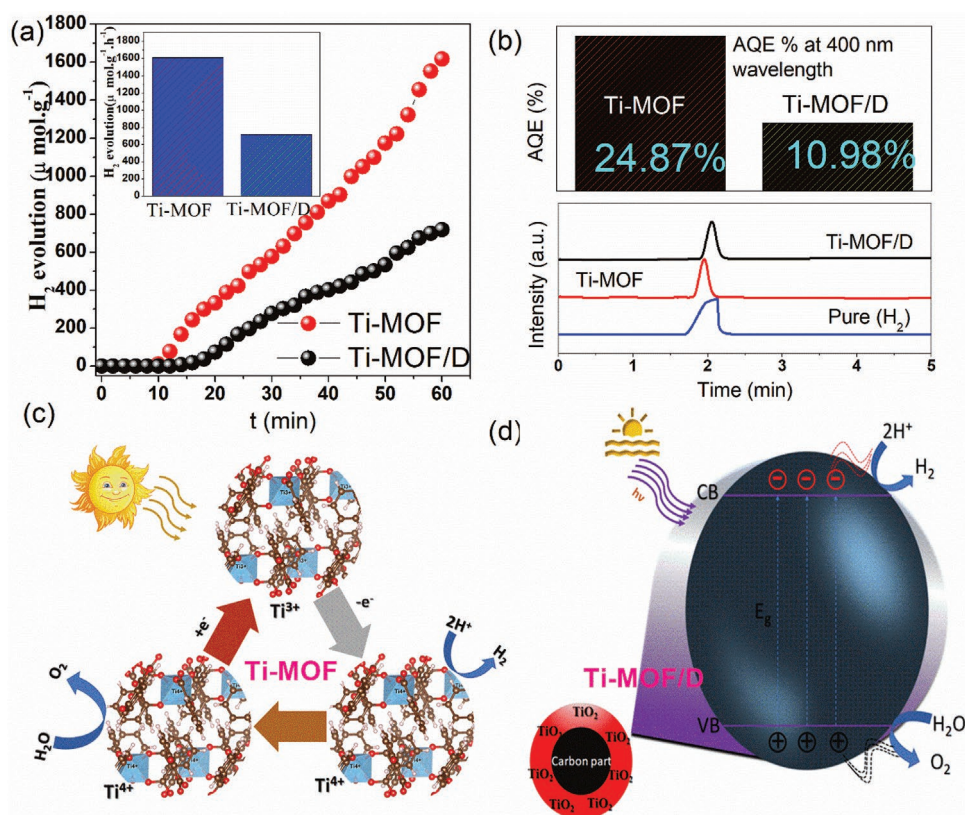
NANO · MICRO
small
www.small-journal.com

Figure 6. Photocatalytic hydrogen evolution and mechanism study. a) Photocatalytic hydrogen evolution activity of the Ti-MOF and Ti-MOF/D, inset shows the total volume of evolved gases in 1 h. b) AQE% for the photocatalytic hydrogen generation at a wavelength of 400 nm. c) The proposed photocatalytic cycle of H_2 evolution for the Ti-MOF. d) Proposed mechanism for the photocatalytic hydrogen generation at Ti-MOF/D.

surface of the hollow sphere is irradiated by solar light and thus photogenerated electrons migrate to the conduction band by leaving holes in its valence band. Then, the TiO_2 electrons in the conduction band initiate the redox reaction and generate hydrogen as shown in Figure 6d. The observed decrease in recombination rates of the electron-hole pairs as seen in the PL measurements (Figure 5d) supports the obtained results. This result also can agree with the interpretation that the partially decomposed organic moiety is present in the inner core of the Ti-MOF/D hollow sphere that cannot easily interfere with the photogenerated charge recombination.

The electrocatalytic performance of Ti-MOF and the annealed Ti-MOF/D samples for hydrogen generation (cathodic half reaction of water splitting on a glassy carbon macrodisc electrode) was studied in 1 M NaOH as electrolyte using the typical three-electrode system. The images of electrodes and the catalytic system are shown in Figure S5 in the Supporting Information and the corresponding movie (Movie S1, Supporting Information) demonstrates the abundance in the rate of H_2 gas bubbles generated at the cathode. According to the Tafel polarization study (**Figure 7**a), the Ti-MOF showed lower potential compared with the Ti-MOF/D at 223 and 298 mV, respectively, at 10 mA cm^{-2} current density indicating the higher catalytic efficiency from the Ti-MOF during HER. The linear sweep voltammetry curve in Figure 7b supports the Tafel polarization data.

The lower onset potential of the cyclic voltamogramms data for the Ti-MOF further confirms the higher electrocatalytic activity toward HER than the annealed Ti-MOF/D sample (Figure 7c).

In alkaline media, the HER pathway could be associated with the Volmer–Heyrovsky or Volmer–Tafel routes, as shown in Figure 7d. The adsorption of water molecules involves both pathways along with the electrochemical reduction into adsorbed H and OH$^-$, and desorption of H_2. Here, comparatively higher catalytic HER from the Ti-MOF is attributed to its optimal structural characteristics for electrocatalysis such as exposed molecular metal active sites and improved electrical conductivity (Figure 7e) within the metal–organic framework. On the other hand, metal oxides/hydroxides are active catalytic centers with limited exposed metal active sites.[24] Therefore, the decreasing catalytic activity in the Ti-MOF/D is due to the rigid outer surface of TiO_2 although the available surface area of the Ti-MOF/D is seven times higher than that of the Ti-MOF. Remarkably, the highly exposed Ti-metal active sites in the Ti-MOF are less hydrophobic compared to the Ti-MOF/D, as suggested by the zeta potential study (Figure 4b,d) which also additionally leads to adsorption of water into the electrode surface and promotes the kinetics of water dissociation.[25]

For a deeper understanding of the electrocatalytic HER performance, the intrinsic charge transfer takes place at the electrode/electrolyte interface is studied using electrochemical impedance spectroscopic technique. Figure 7e shows the
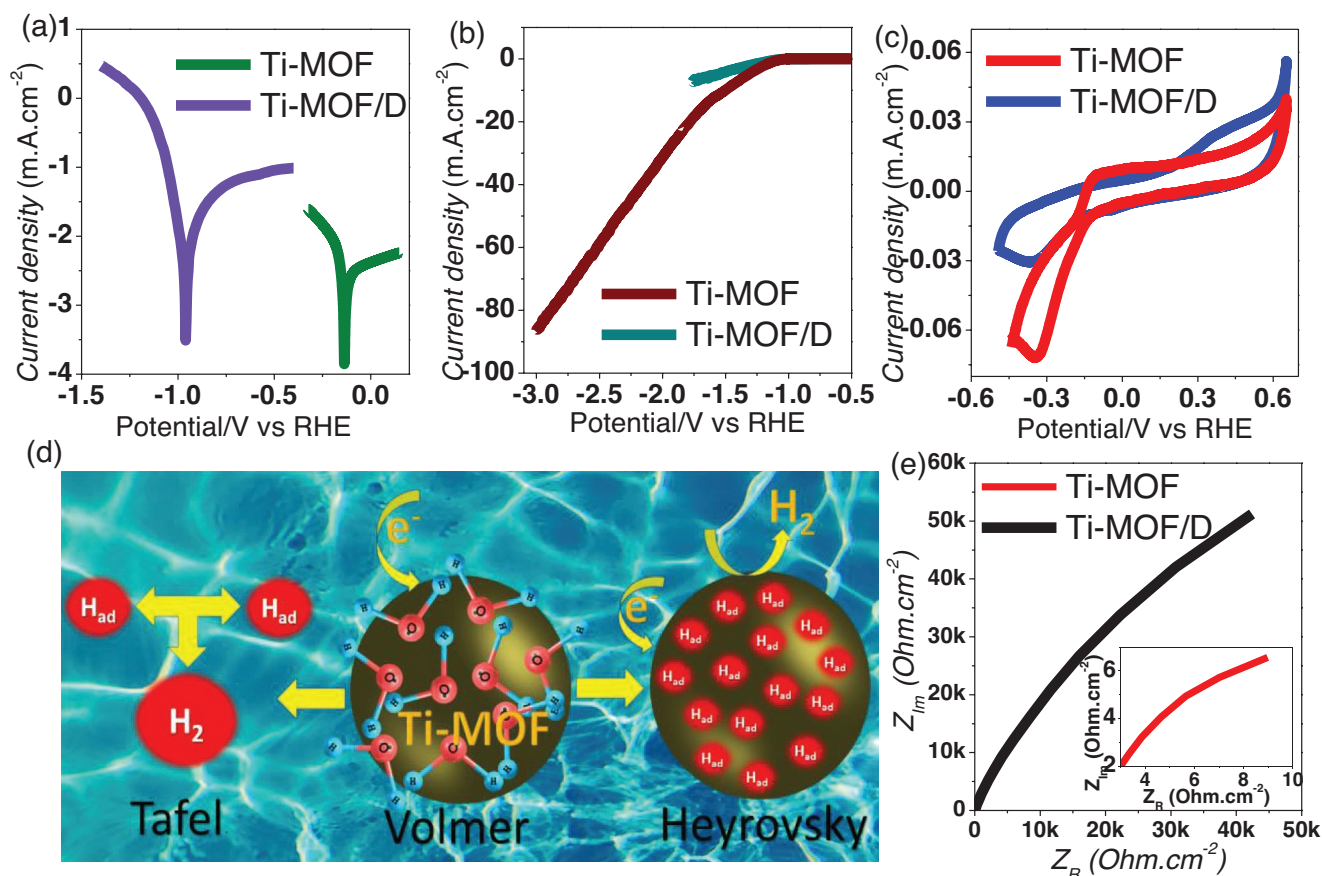
ADVANCED
SCIENCE NEWS
www.advancedsciencenews.com

NANO · MICRO
small
www.small-journal.com

Figure 7. Electrocatalytic HER for the Ti-MOF and annealed Ti-MOF/D sample. a) Polarization curves, b) linear sweep voltammetry curves, c) cyclic voltammetric curves obtained from the Ti-MOF and Ti-MOF/D for HER at 10 mV^{-1} in 1 M NaOH. d) The possible mechanism involves hydrogen evolution in an alkaline medium. e) Electrochemical impedance spectroscopy.

obtained semicircles electrochemical impedance for both samples whereas the equivalent circuit is shown in Figure S6 in the Supporting Information. Nyquist findings were substantiated by Bode plots shown in Figure S7 in the Supporting Information. The details explanation and data for electrochemical studies are presented in the Supporting Information. It can be seen from the figures that the Ti-MOF showed much lower charge transfer resistance at the electrode/electrolyte interface compared to that of the Ti-MOF/D. This result is very surprising as MOFs usually have poor electrocatalytic activities.[2a] This phenomenon could be attributed to the improved charge separation induced by optimal exposed Ti-active sites as well as enhanced water oxidation kinetics that is absent in the Ti-MOF/D due to the rigid TiO$_2$ outer layer. In general, materials with larger specific surface area are rich in electrochemically as well as photochemically active catalytic sites and show better performance of hydrogen evolution. In the present case, the surface modified Ti-MOF/D obviously revealed high specific surface area as compared to pure Ti-MOF due to the generation of more number of pores during low temperature annealing. However, this did not significantly increase the catalytically active sites. This was also supported by electrochemical impedance spectroscopy (EIS) data (Figure 7e). The double layer capacitance value is directly proportional to the catalytically active sites that is higher for Ti-MOF as compared to Ti-MOF/D.

4. Conclusions

The effect of partial disintegration of organic ligands in Ti-MOF was selectively studied for photo(electro)catalytic HER. Ti-MOF solid structure was rationally fabricated via a one-pot synthetic protocol and corresponding core–shell Ti-MOF/D hollow spheres was designed by annealing. The surface area of the Ti-MOF/D was seven times higher than that of the Ti-MOF but the photocatalytic HER activity of the Ti-MOF is comparatively higher. The Ti-MOF could initiate other electronic transitions such as (L-M, M-L) charge transfer and d–d transition that leads to an enlarged absorption response compared to the Ti-MOF/D. The characteristics features of the Ti-MOF enhanced light absorption ability, improved migration efficiency and charge separation, suppressed photogenerated electron–hole pairs and activate the active sites for effective photoredox catalysis. Similarly, electrocatalytic HER for the Ti-MOF is attributable to its optimal structural characteristics such as exposed molecular metal active sites and improved electrical conductivity. However, the rigid layer of TiO$_2$ on the outer surface reduces the interaction with the partially disintegrated organic moiety that creates a fence to enhance the catalytic activity. These unique features of the materials will be of great benefit to material scientists for designing novel materials by manipulating them in the nanometer range using this effective way of synthesis.

5. Experimental Section

Synthesis: 1 mmol of Ti-isopropoxide was dissolved with 2 mmol of salicylic acid initially in 50 mL of ethanol and the mixture was stirred. Afterward, the mixture was transferred into 100 mL Teflon-lined stainless-steel autoclave and placed in a preheated air-oven and heated at 180 °C for 20 h and then cooled down at room temperature. The precipitate was washed with ethanol and dried at 60 °C overnight in a hot air oven. The obtained precipitate is donated as Ti-MOF. The as-obtained Ti-MOF was annealed at 350 °C for 15 min under air atmosphere and was denoted as Ti-MOF/D.

Characterization: The XRD patterns of the prepared samples was studied using XRD, Philips X' Pert Materials Powder Diffractometer X-ray powder diffractometer with Cu-K_λ (λ = 1.540 Å) radiation. The presence of functional groups has been studied using FTIR (Shimadzu IR Prestige 21). The elemental composition and particle distribution were investigated by energy dispersive X-ray analysis and elemental mapping, respectively. FESEM (Nova nano SEM 450) and HRTEM (Joel/JEM2100) were used to study the morphology and microstructure of the materials. The average particle size distribution and the zeta potential were obtained using a nanoparticle analyzer (HORIBA Scientific, SZ-100). XPS (Thermo ESCALAB 250i XPS, Al K_α, h_υ: 1486.6 eV) was used to analyze the surface composition and chemical states of the materials. Textural porosity and specific surface area were obtained by BET analysis (AutosorbiQ Station 1). The UV-visible light absorption spectra was recorded using a UV-visible diffused reflectance spectroscopy (Schimadzu UV-2450 analyzer) and the PL studies are carried out with HITACHI-FL 700 instrument after initially exciting the samples at 220 nm.

Photo(electro)catalytic Measurements: At room temperature, the photocatalytic activity was performed under solar light irradiation using a Solar Simulator (AAA, Solar light line A1, Science Tech. Pvt. Ltd.). Here, the illumination intensity is equal to the one sun intensity (100 mW cm^{-2}). Previously, it was described in detail about experimental setup and calculation of the AQE.[26] The electrocatalytic HER has been studied in 1 м NaOH electrolyte solution at room temperature using an electrochemical workstation (Biologic SP-200) using a three electrodes system (Hg/HgO/OH$^-$, Pt and studied sample grown on glassy carbon macrodisc electrode as the reference, counter and working electrodes respectively). Further details of the system can be found in ref. [27].

Supporting Information

Supporting Information is available from the Wiley Online Library or from the author.

Acknowledgements

Conflict of Interest

The authors declare no conflict of interest.

Data Availability Statement

Research data are not shared.

Keywords

[1] a) L. Chen, X. Zhang, X. Cheng, Z. Xie, Q. Kuang, L. Zheng, *Nanoscale Adv.* **2020**, *2*, 2628; b) C. Wang, X. Liu, N. Keser Demir, J. P. Chen, K. Li, *Chem. Soc. Rev.* **2016**, *45*, 5107.

[2] a) L. Zhang, P. Cui, H. Yang, J. Chen, F. Xiao, Y. Guo, Y. Liu, W. Zhang, F. Huo, B. Liu, *Adv. Sci.* **2016**, *3*, 1500243; b) Y. Pi, X. Feng, Y. Song, Z. Xu, Z. Li, W. Lin, *J. Am. Chem. Soc.* **2020**, *142*, 10302; c) J. Duan, S. Chen, C. Zhao, *Nat. Commun.* **2017**, *8*, 15341.

[3] a) L. Sun, M. G. Campbell, M. Dincă, *Angew. Chem., Int. Ed.* **2016**, *55*, 3566; b) D. Sheberla, J. C. Bachman, J. S. Elias, C.-J. Sun, Y. Shao-Horn, M. Dincă, *Nat. Mater.* **2017**, *16*, 220.

[4] a) H. Razavi-Khosroshahi, K. Edalati, M. Hirayama, H. Emami, M. Arita, M. Yamauchi, H. Hagiwara, S. Ida, T. Ishihara, E. Akiba, Z. Horita, M. Fuji, *ACS Catal.* **2016**, *6*, 5103; b) J. Sun, N. Guo, Z. Shao, K. Huang, Y. Li, F. He, Q. Wang, *Adv. Energy Mater.* **2018**, *8*, 1870121; c) W. Xie, R. Li, Q. Xu, *Sci. Rep.* **2018**, *8*, 8752.

[5] G. Prieto, H. Tüysüz, N. Duyckaerts, J. Knossalla, G.-H. Wang, F. Schüth, *Chem. Rev.* **2016**, *116*, 14056.

[6] L. Zhou, Z. Zhuang, H. Zhao, M. Lin, D. Zhao, L. Mai, *Adv. Mater.* **2017**, *29*, 1602914.

[7] F. You, J. Wan, J. Qi, D. Mao, N. Yang, Q. Zhang, L. Gu, D. Wang, *Angew. Chem., Int. Ed.* **2020**, *59*, 721.

[8] M. Sayed, F. Xu, P. Kuang, J. Low, S. Wang, L. Zhang, J. Yu, *Nat. Commun.* **2021**, *12*, 4936.

[9] a) A. Hossain, K. Sakthipandi, A. K. M. Atique Ullah, S. Roy, *Nano-Micro Lett.* **2019**, *11*, 103; b) P. Jineesh, A. Hossain, J. Ahmed, S. M. Alshehri, Y. Mao, S. M. A. Shibli, *J. Alloys Compd.* **2022**, *903*, 163813; c) P. Jineesh, A. Hossain, R. Remya, J. N. Sebeelamol, R. K. Manavalan, J. Ahmed, M. S. Tamboli, S. M. A. Shibli, *Ceram. Int.* **2022**, *48*, 15026.

[10] S. Chooset, A. Kantacha, K. Chainok, S. Wongnawa, *Inorg. Chim. Acta* **2018**, *471*, 493.

[11] C. Wang, Y. Wang, Y. Dang, Q. Jiao, H. Li, Q. Wu, Y. Zhao, *Russ. J. Appl. Chem.* **2015**, *88*, 1723.

[12] a) Z. Jiang, H. Sun, T. Wang, B. Wang, W. Wei, H. Li, S. Yuan, T. An, H. Zhao, J. Yu, P. K. Wong, *Energy Environ. Sci.* **2018**, *11*, 2382; b) J. Liu, S. Z. Qiao, S. Budi Hartono, G. Q. Lu, *Angew. Chem., Int. Ed.* **2010**, *49*, 4981.

[13] a) Y. Chimupala, G. Hyett, R. Simpson, R. Mitchell, R. Douthwaite, S. J. Milne, R. D. Brydson, *RSC Adv.* **2014**, *4*, 48507; b) J. Vishakantaiah, P. Singh, K. P. Reddy, *Adv. Ceram. Sci. Eng. (ACSE) February 2013* **2013**, *2*, 40.

[14] a) J. Guan, F. Mou, Z. Sun, W. Shi, *Chem. Commun.* **2010**, *46*, 6605; b) H. Hwang, H. Shin, W.-J. Lee, *Sci. Rep.* **2017**, *7*, 46378; c) G. D. Park, J.-H. Lee, J.-K. Lee, Y. C. Kang, *Nano Res.* **2014**, *7*, 1738.

[15] S. Khashan, S. Dagher, N. Tit, A. Alazzam, I. Obaidat, *Surf. Coat. Technol.* **2017**, *322*, 92.

[16] a) X. Yang, K. Fan, Y. Zhu, J. Shen, X. Jiang, P. Zhao, C. Li, *J. Mater. Chem.* **2012**, *22*, 17278; b) Q. Zhang, H. Chen, X. Han, J. Cai, Y. Yang, M. Liu, K. Zhang, *ChemSusChem* **2016**, *9*, 186.

[17] F. Amano, K. Nogami, M. Tanaka, B. Ohtani, *Langmuir* **2010**, *26*, 7174.

[18] S. Sun, H. Li, Z. J. Xu, *Joule* **2018**, *2*, 1024.

[19] R. Singh, M. K. Tiwari, D. Gangopadhyay, P. C. Mishra, H. Mishra, A. Srivastava, R. K. Singh, *J. Photochem. Photobiol., B* **2018**, *189*, 292.

[20] Q. Ma, X. Lv, Y. Wang, J. Chen, *Opt. Mater.* **2016**, *60*, 86.

[21] a) B. Dai, J. Fang, Y. Yu, M. Sun, H. Huang, C. Lu, J. Kou, Y. Zhao, Z. Xu, *Adv. Mater.* **2020**, *32*, 1906361; b) Y.-P. Zhu, J. Yin, E. Abou-Hamad, X. Liu, W. Chen, T. Yao, O. F. Mohammed, H. N. Alshareef, *Adv. Mater.* **2020**, *32*, 1906368.

[22] J. C. Yu, H. Yu, Z. Jiang, *Chem. Mater.* **2002**, *14*, 3808.

[23] P. Kuang, M. Sayed, J. Fan, B. Cheng, J. Yu, *Adv. Energy Mater.* **2020**, *10*, 1903802.

[24] J. Luo, J.-H. Im, T. Mayer Matthew, M. Schreier, K. Nazeeruddin Mohammad, N.-G. Park, S. D. Tilley, J. Fan Hong, M. Grätzel, *Science* **2014**, *345*, 1593.

[25] S. Chen, J. Duan, M. Jaroniec, S. Z. Qiao, *Angew. Chem., Int. Ed.* **2013**, *52*, 13567.

[26] M. S. Meera, S. K. Sasidharan, A. Hossain, J. Kiss, Z. Kónya, L. Elias, S. M. A. Shibli, *ACS Appl. Energy Mater.* **2022**, *5*, 3578.

[27] V. S. Sumi, M. A. Sha, S. R. Arunima, S. M. A. Shibli, *Electrochim. Acta* **2019**, *303*, 67.